Astrophys Space Sci (2007) 307: 399–407
DOI 10.1007/s10509-007-9388-9

ORIGINAL ARTICLE

Turbulent compressible convection with rotation–penetration below a convection zone

Partha S. Pal · Harinder P. Singh · Kwing L. Chan · M.P. Srivastava

Received: 31 October 2006 / Accepted: 19 January 2007 / Published online: 10 March 2007

Abstract We examine the behaviour of penetrative turbulent compressible convection under the influence of rotation by means of three dimensional numerical simulations. We estimate the extent of penetration below a stellar-type rotating convection zone in an f-plane configuration. Several models have been computed with a stable-unstable-stable configuration by varying the rotation rate ($\mathbf{\Omega}$), the inclination of the rotation vector and the stability of the lower stable layer. The spatial and temporal average of kinetic energy flux ($\mathrm{F_k}$) is computed for several turnover times after the fluid has thermally relaxed and is used to estimate the amount of penetration below the convectively unstable layer. Our numerical experiments show that with the increase in rotational velocity, the downward penetration decreases. A similar behaviour is observed when the stability of the lower stable layer is increased in a rotating configuration. Furthermore, the relative stability parameter S shows an $S^{-1/4}$ dependence on the penetration distance implying the existence of a thermal adjustment region in the lower stable layer rather than a nearly adiabatic penetration region.

Keywords Convection—stars · Interior—Sun · Interior—rotation

P.S. Pal · H.P. Singh (✉) · M.P. Srivastava
Department of Physics & Astrophysics, University of Delhi, Delhi 110 007, India
e-mail: hpsingh@physics.du.ac.in

K.L. Chan
Department of Mathematics, Hong Kong University of Science & Technology, Hong Kong, China

1 Introduction

Three-dimensional Direct Numerical Simulations (DNS) of turbulent compressible convection in stellar type convection zones promise to provide a deeper understanding of the general behaviour of convective transport of energy from scales ranging from the size of the convection zone itself to the smallest scales which can be of the order of one meter or less in a star like Sun. Although some attempts have been made to study the upper shallower layers of solar or stellar type convection zones by means of realistic simulations with some degree of success (Stein and Nordlund 1991; Rast et al. 1991), we are still far away from fully resolving the flows close to the bottom of the convection zones. This is because the speed and memory requirements of the problem are too enormous to be handled by the present generation of computers (Chan and Sofia 1986, 1996; Brummell et al. 1996; Singh and Chan 1993; Singh et al. 1994).

Large Eddy Simulations (LES) of convection have been widely employed to study deep convection in stellar interiors. These simulations attempt to model the large scale flows explicitly while the smaller scales are modeled by some sort of sub-grid-scale formulation (Smagorinsky 1963; Chan and Sofia 1986; Hossain and Mullan 1991, 1993; Muthsam et al. 1995; Singh et al. 1995, 1998a, 1998b). These simulations can have a coarser grid and hence are less intensive in terms of their speed and memory requirements.

Recently, a region in the solar interior called tachocline has invoked much interest. Helioseismic inversion technique have inferred that this thin transition region exists between the differentially rotating convection zone and the rigid rotating radiative region below (Thomson et al. 1996). This region has been named tachocline owing to a strong gradient in angular velocity there (Spiegel 1972; Spiegel and Zahn

1992). The underlying dynamics of tachocline is poorly understood both observationally and theoretically (Chan 2001; Brummell et al. 2002). It is also expected that the interaction of the tachocline with the convectively unstable region will affect the mixing of material and evolution of magnetic field at base of the convective zone.

Simulations of penetrative convection have been performed in two dimensions for a non-rotating configuration by Roxburgh and Simmons (1993), Hurlburt et al. (1994) and Freytag et al. (1996). Hurlburt et al. systematically increased the stability of the lower stable layer and gave some scaling laws relating the penetration distance and the relative stability (S) of the unstable to the stable zone. Three-dimensional simulations of penetrative convection have been studied by Singh et al. (1994, 1995), Muthsam et al. (1995), Singh et al. (1996, 1998a, 1998b), Saikia et al. (2000). Brummell et al. (2002) extended the study by including the effects of rotation into their 3D simulation model. They calculated several models and found that in all the cases motions from the convective region overshoot a significant fraction of pressure scale height into the stable layer below. Further, they reported that the penetrative region is not adiabatic even in models with the highest rms flow velocities. The penetration depth follows the scaling $\Delta_p \sim S^{-1/4}$ approximately, thereby implying a thermal adjustment region below the convection zone as per the theory presented in Hurlburt et al. (1994). In addition, Brummell et al. (2002) also studied the effect of rotation on the penetrative behaviour and concluded that the inclusion of rotation led to a breaking of the downward flows resulting in a decrease in the penetration distance.

In this paper, we perform large eddy simulations of turbulent convection by including rotation in an f-plane configuration with a view to study the effect of rotation on the penetration distance. We compute a total of 13 models to see the effect of rotation rate ($\boldsymbol{\Omega}$) and the colatitude (θ) on the penetration distance. In some of the models we systematically vary the stability parameter (S) to see whether the penetration proceeds adiabatically or by way of a thermal adjustment region as claimed by Brummell et al. (2002) for rotating convection zones. In Sect. 2, we provide the parameters for the 13 computed cases together with the equations of the problem. In Sect. 3, we present the results together with a discussion of the results. In Sect. 4, we summarize the important conclusions of the study.

2 Parameters of computed models

We study the effects of rotation on penetrative behaviour of turbulent compressible convection in a stellar-type convection zone. The Naviér-Stokes equations are numerically solved and rotational effects are incorporated using an f-plane configuration. A plane parallel layer of perfect gas is considered in a rectangular box which defines the domain of computation as shown in Fig. 1 and can be viewed as small portion of a spherical shell. The aspect ratio (width/depth) of the box is fixed at 1.5. The shell rotates around the polar axis and the angular velocity vector $\boldsymbol{\Omega}$ points toward the north pole. We adopt a Cartesian coordinate system with X increasing to the south and Y increasing to the east. The upward vertical direction is denoted by Z and the gravity vector $\boldsymbol{g}$ is along the negative Z direction. The configuration is similar to that of Chan (2001). The angle between $\boldsymbol{\Omega}$ and the Z-axis is denoted by θ and is the same as the colatitude (=90°-latitude) of the box in the shell. The tilted rotation vector $\boldsymbol{\Omega}$ lies in the XZ plane and is considered constant implying a uniform angular velocity of the sphere. In the rotating frame, the equations representing the stratified compressible hydrodynamical flow are:

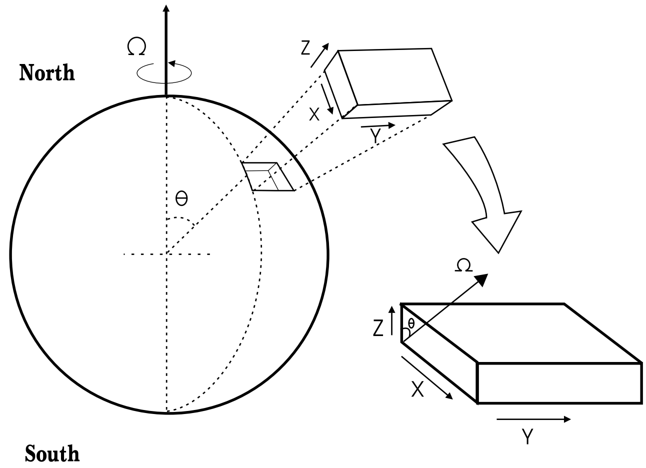

Fig. 1 f-plane configuration in which the angular velocity vector $\boldsymbol{\Omega}$ points toward the north pole. The angle between $\boldsymbol{\Omega}$ and the Z-axis is θ which is also the colatitude (90°-latitude). The coordinates X and Y are along the north-to-south (meridional) and west-to-east (zonal) directions, respectively. The *upward vertical direction* is denoted by Z and the tilted rotation vector $\boldsymbol{\Omega}$ lies in the XZ plane

$$\partial_t \rho = -\nabla \,.\, (\rho \boldsymbol{v}), \tag{1}$$

$$\partial_t \rho \boldsymbol{v} = -\nabla \,.\, (\rho \boldsymbol{v}\boldsymbol{v}) - \nabla p + \nabla \,.\, \boldsymbol{\Sigma} + \rho \boldsymbol{g} + 2\rho \boldsymbol{v} \times \boldsymbol{\Omega}, \tag{2}$$

$$\partial_t E = -\nabla \,.\, \{(E+p)\boldsymbol{v} - \boldsymbol{v} \,.\, \boldsymbol{\Sigma} + \mathbf{F_d}\} + \rho \boldsymbol{v} \,.\, \boldsymbol{g}, \tag{3}$$

where ρ is the density, v is the velocity with components v_x, v_y and v_z, (ρv) is the mass flux vector, $E = e + \rho v^2/2$ is the total energy density, e is the internal energy, p is the gas pressure and $\mathrm{F_d}$ is the diffusive heat flux. Σ is the viscous stress tensor which has the form

$$\boldsymbol{\Sigma} = 2\mu\sigma + \lambda(\nabla \,.\, \boldsymbol{v})\boldsymbol{I}, \tag{4}$$

where μ and λ are the first and bulk viscosity coefficients, respectively and $\boldsymbol{I}$ is the identity tensor. The effects of turbulence are accounted for by the Sub-Grid-Scale (SGS) eddy viscosity represented by

$$\mu = \rho (c_\mu \Delta)^2 (2\sigma : \sigma)^{1/2}, \tag{5}$$

where c_μ is the Deardorff coefficient (Smagorinsky 1963; Deardorff 1971), σ is the strain rate tensor and the colon sign inside the bracket denotes tensor contraction and $\Delta^2 = (\Delta_x \Delta_y)^{1/2} \Delta_z$. The SGS turbulent diffusivity is computed from this viscosity by assuming a constant Prandtl number $\mathrm{Pr} = 1/3$. The diffusive heat flux $\mathrm{F_d}$ in the energy equation (3), is a part of total flux F which is made up of enthalpy, kinetic energy, viscous and diffusive fluxes:

$$\mathbf{F} = \mathbf{F_e} + \mathbf{F_k} + \mathbf{F_v} + \mathbf{F_d}, \tag{6}$$

with

$$\mathbf{F_e} = (e + p)\boldsymbol{v}, \tag{7}$$

$$\mathbf{F_k} = (\rho V^2/2)\boldsymbol{v}, \tag{8}$$

$$\mathbf{F_v} = -\boldsymbol{v} \,.\, \Sigma, \tag{9}$$

$$\mathbf{F_d} = -K_T \nabla T - K_s \nabla s, \tag{10}$$

where s is the specific entropy given by

$$s = \gamma \ln T/(\gamma - 1) - \ln p, \tag{11}$$

γ is the ratio of specific heats (C_p/C_v) and is taken $5/3$. Our computational domain is divided into three layers with the convective middle layer embedded between a stable layer above and below. The stable-unstable-stable configuration is generated by controlling the conductivities of the diffusive flux $\mathrm{F_d}$ (Singh et al. 1994, 1995; Chan 2001). In (10), the first term represent radiative diffusion while the second term represent energy diffusion through the sub-grid-scale turbulence. In the stable layers K_s is set to zero while K_T is taken as $\mathrm{F_b}/|\nabla T| = \mathrm{F_b}(m+1)/g$, where m is the polytropic index. In the unstable middle layer K_T is set close to zero while K_s is given by $\mu T/\mathrm{Pr}$, where Pr is the effective Prandtl number of the SGS turbulence.

To express our equations for various layers conveniently, we have numbered the three regions, starting with the lower stable layer as 1, the middle unstable layer as 2 and the upper stable layer as 3. The depths z_{12} and z_{23} refer to the interfaces of the layers 1 and 2 and layers 2 and 3, respectively. Also, we use subscripts b and t to define various thermodynamic quantities at the bottom z_1 and top z_3 of the domain, respectively. The temperature, density and pressure for the initial stratification in each layer of a perfect gas under the influence of constant gravitational acceleration can be expressed in terms of the polytropic index (m). Thus we have in the top layer:

$$T = T_t + \frac{g}{m_3 + 1}(z_3 - z); \qquad p = p_t \left(\frac{T}{T_t}\right)^{m_3+1}, \tag{12}$$

in the middle layer:

$$T = T_{23} + \frac{g}{m_2 + 1}(z_{23} - z); \qquad p = p_{23} \left(\frac{T}{T_{23}}\right)^{m_2+1}, \tag{13}$$

in the bottom later:

$$T = T_{12} + \frac{g}{m_1 + 1}(z_{12} - z); \qquad p = p_{12} \left(\frac{T}{T_{12}}\right)^{m_1+1}, \tag{14}$$

where $\rho = p/T$ is the density. The finite-difference grid contains $35 \times 35 \times 51$ points and is uniform in the two horizontal directions. The vertical grid spacing decreases smoothly with height (Singh et al. 1995). The aspect ratio (width/depth) of the box is set to 1.5. Also, all the thermodynamic variables are expressed in units which set the total depth and initial density, pressure and temperature at the top to 1. This is achieved by scaling variables using a length scale and ρ_t, p_t, T_t. For example, the velocities v are scaled to $(p_t/\rho_t)^{1/2}$ and various energies are scaled to p_t. The scaling for various fluxes including the input flux $\mathrm{F_b}$ is $(p_t v_t)$. The equations are solved using an implicit scheme (Chan and Wolff 1982) and the time step is characterized by the CFL number

$$N_{\mathrm{CFL}} = C_s \Delta t / \Delta_{\min}, \tag{15}$$

where $\Delta_{\min}$ is the minimum grid size in any direction and $C_s = \gamma^{1/2}$ is the dimensionless sound speed at the top. The boundary conditions imposed are:

$$\mathrm{F_b} = \mathrm{const} = 0.125 \quad \text{(at the bottom)},$$

$$T = T_t = \mathrm{const} \quad \text{(at the top)},$$

$$v_z = 0; \qquad \frac{\partial v_x}{\partial z} = \frac{\partial v_y}{\partial z} = 0.$$

The top and bottom boundaries are, then, impenetrable and slippery while the side boundaries are periodic. Although the spatial resolution is low, several models are computed, each taking a few million steps before the thermal relaxation sets in. Our models show considerable similarity with the high resolution calculations of Brummell et al. (2002). Also, our earlier calculations (Chan and Sofia 1986, 1989; Singh et al. 1994, 1995, 1998a, 1998b; Chan 2001, 2003) show that such a resolution is adequate for the problem under investigation. Käpylä et al. (2005) have studied the dependence of mixing length relations on the resolution by changing the number of grid points from 64^3 to 256^3. Although their 256^3 calculation is not fully thermally relaxed, they conclude that the qualitative results remain unchanged as a function of resolution.

Table 1 Common physical parameters for models S1 to S10

Grid	F_b	Polytropic Indices			P_b	T_b	ρ_b	Layer Thickness (in PSH)		
		Top	Middle	Bottom				Top	Middle	Bottom
$35 \times 35 \times 51$	0.125	1.5	1.5	2.0	2042	19.45	105.0	1.13	5.27	1.22

Table 2 Physical parameters for models S11 to S13

Model	Grid	F_b	Polytropic Indices			P_b	T_b	ρ_b	Layer Thickness (in PSH)		
			Top	Middle	Bottom				Top	Middle	Bottom
S11	$35 \times 35 \times 51$	0.125	1.5	1.5	3.0	2163	18.37	117.7	1.20	5.44	1.02
S12	$35 \times 35 \times 51$	0.125	1.5	1.5	4.0	2246	17.38	129.2	1.24	5.44	1.01
S13	$35 \times 35 \times 51$	0.125	1.5	1.5	5.0	2306	16.71	138.1	1.26	5.43	1.03

Table 3 Numerical parameters for the 13 models

Models	g	C_μ	Δt	t	N_{CFL}	$\Delta_{\min}$
S1–S10	50	0.2	0.001262	1893	0.1	0.01629
S11–S13	50	0.2	0.001262	3786	0.1	0.01629

We have computed 13 models and the physical parameters for the models are listed in Tables 1, 2, and 4. The numerical parameters of the simulations are given in Table 3. As may be noticed, models S11 to S13, have been evolved for a longer time as they require longer integration for thermal relaxation. Columns (6–9) in Table 4 list the values of Coriolis number (Co), Rossby number (Ro), effective Reynolds number (Re), and Taylor number (Ta) for the simulated cases. Following Chan (2001), they are defined as

$$Co = \boldsymbol{\Omega} d/\langle v''\rangle,$$

$$Ro = 1/Co,$$

$$Re = \langle v''\rangle d/\langle \bar{\mu}/\bar{\rho}\rangle,$$

$$Ta = (2\boldsymbol{\Omega} d^2/\langle \bar{\mu}/\bar{\rho}\rangle)^2,$$

with $v'' \equiv (v_x''^2 + v_y''^2 + v_z''^2)^{1/2}$ where v_x'' denotes the root mean square (rms) fluctuation of v_x etc. The extent of domain is denoted by d.

Models S1 to S10 are computed to examine the effect of rate of rotation ($\boldsymbol{\Omega}$) and the angle (θ) between the rotation vector and the vertical axis on the extent of penetration below the convectively stable layer. The polytropic index of the lower stable layer is taken to be 2.0 in models S1 to S4, $\boldsymbol{\Omega}$ is varied from 0 to 1.0 while θ is fixed at 0°. In the second set of models S5 to S8, θ is varied from to 22.5° to 90° keeping $\boldsymbol{\Omega}$ fixed at 0.25. In models S9 and S10, $\boldsymbol{\Omega}$ is 0.5 and 1.0, respectively while θ is fixed at 45°. In the last set of models S11 to S13, polytropic index of the lower stable layer is varied from 3 to 5 while all the other parameters are the same as model S9.

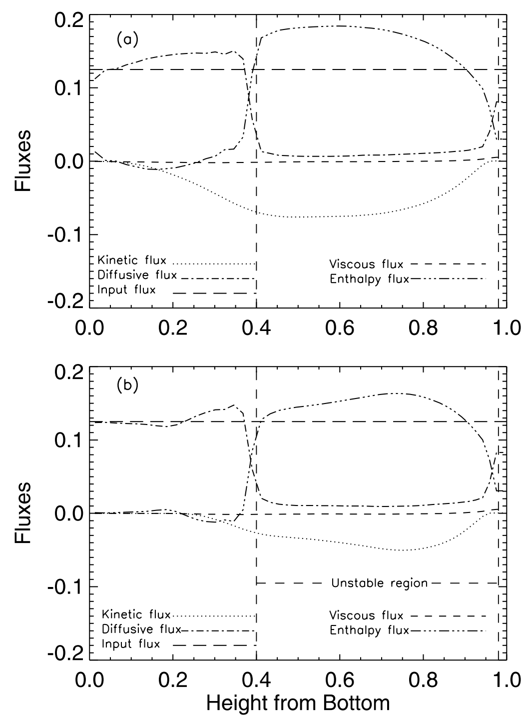

Fig. 2 *Vertical profiles* of the time and *horizontally* averaged energy fluxes for (**a**) case S1 ($\boldsymbol{\Omega} = 0$, $\theta = 0°$), (**b**) case S9 ($\boldsymbol{\Omega} = 0.5$, $\theta = 45°$)

Models S9, S11, S12 and S13 have been setup to examine the effect of stability of the lower stable layer on the penetration depth of these rotating configurations. These four models are distinguished from each other by the value of the polytropic index in the lower stable layer, namely, 2, 3, 4 and 5 for the cases S9, S11, S12 and S13, respectively. For all these four models, the values of $\boldsymbol{\Omega}$ and θ are kept constant at 0.5 and 45° respectively. It is convenient to de-

Table 4 Dynamical parameters of the computed models

Model	$\boldsymbol{\Omega}$	θ/π	θ	$\langle v'' \rangle$	Co	Ro	Re	Ta	Δ_d	Δ_p (PSH)
S1	0	0	0°	0.188	0.000	∞	645	0.00E+0	0.349	1.08
S2	0.25	0	0°	0.182	1.373	0.728	630	3.00E+6	0.214	0.71
S3	0.50	0	0°	0.177	2.824	0.354	611	1.19E+7	0.179	0.61
S4	1.0	0	0°	0.170	5.882	0.170	599	4.97E+7	0.152	0.52
S5	0.25	1/8	22.5°	0.186	1.344	0.744	632	2.89E+6	0.244	0.80
S6	0.25	1/4	45°	0.189	1.322	0.756	646	2.92E+6	0.234	0.77
S7	0.25	3/8	67.5°	0.193	1.295	0.772	655	2.88E+6	0.277	0.89
S8	0.25	1/2	90°	0.195	1.282	0.780	660	2.86E+6	0.315	0.99
S9	0.50	1/4	45°	0.190	2.631	0.380	643	1.15E+7	0.179	0.61
S10	1.0	1/4	45°	0.179	5.586	0.179	611	4.66E+7	0.125	0.44
S11	0.50	1/4	45°	0.186	2.688	0.372	638	1.17E+7	0.109	0.38
S12	0.50	1/4	45°	0.175	2.857	0.350	611	1.22E+7	0.082	0.29
S13	0.50	1/4	45°	0.180	2.777	0.360	632	1.23E+7	0.077	0.28

fine a relative stability parameter S (Hurlburt et al. 1994; Singh et al. 1995) for the four cases. We write,

$$S = \frac{m_i - m_a}{m_2 - m_a}; \quad i = 2, 3, 4, 5, \tag{16}$$

where m_i denote the polytropic indices of the lower stable layer for various cases, m_2 is the polytropic index of the lower stable layer for our case S9 and $m_a = 1/(\gamma - 1)$ is the adiabatic index. Here we have taken $\gamma = C_p/C_v$ as $5/3$. Thus for our reference case S9 the relative stability parameter S is equal to unity and for cases S11, S12 and S13 it comes out to be 3, 5 and 7, respectively.

3 Results and discussion

All 13 models computed in this study have a three layer configuration in which the convectively unstable region is sandwiched between two stable layers. The aspect ratio of the numerical box in the f-plane setup is kept at 1.5 for all the cases. Model S1 is non-rotating while models S2 to S13 are all rotating, differentiated by a set of values of rate of rotation ($\boldsymbol{\Omega}$), the angle between the Z-axis and the rotation vector (θ) and the polytropic index of the lower stable layer. The physical parameters of all the models are listed in Tables 1 and 2.

The interface of the lower stable layer–unstable layer is located at a height of 0.4 from the bottom (40% of the total domain) and the interface of the unstable–upper layer is located at a height of 0.98 from the bottom (2% of the total domain). There are a total of about 7.5 pressure scale heights (PSH) for models S1–S10 with the upper and lower stable layer containing 1.13 PSH and 1.22 PSH respectively while the middle convective layer contains 5.27 PSH. For models S11–S13 the total domain has around 7.7 PSH with the upper and lower stable layer contain around 1.2 and 1.0 PSH, respectively.

It may be noticed that although the upper stable layer occupies only 2% of the domain, it contains more than 12% of the PSH. This is because the length of the PSH decreases as we go from bottom to the top. The purpose of the upper stable layer in our simulation is to pad the convection zone from the upper solid boundary.

The density contrast ($\rho_{\text{bottom}}/\rho_{\text{top}}$) of models S1–S10 is 105.0 while the temperature contrast ($T_{\text{bottom}}/T_{\text{top}}$) is 19.45 (cf. Table 1). For model S13 the density contrast is the maximum (138.1). For all the models, there is a significant background stratification across the convection zone with density contrast ∼24.

After the fluid has thermally relaxed, it is further evolved for another 5000 time steps and the time and horizontal averages are taken for quantities of interest. The calculation of the extent of the penetration into the lower stable layer has been based on time- and horizontally averaged kinetic flux (F_k). Such a choice is obvious as the kinetic flux is directly related with the motions and the profile is also convenient for estimation of the extent of penetration (Hurlbert et al. 1986, 1994; Singh et al. 1995; Saikia et al. 2000). In Fig. 3 we illustrate this point by plotting the distribution of kinetic energy flux for several sets of models. The kinetic energy flux is negative in all of the convectively unstable region and falls to zero in the lower stable region. Ideally, the extent of penetration should correspond to the first zero of the kinetic energy flux in the lower stable layer below the unstable-stable interface. However, we define the penetration depth (Δ_d) to be the distance from the interface of the unstable-lower stable layer to where F_k has fallen to 1% of its value at the interface. The extent of penetration distance (Δ_d) and penetration distance in PSH (Δ_p) for all the 13 models is given in Table 4.

In order to check whether the fluid is thermally relaxed, we evolved a few models for 1,00,000 steps and estimated

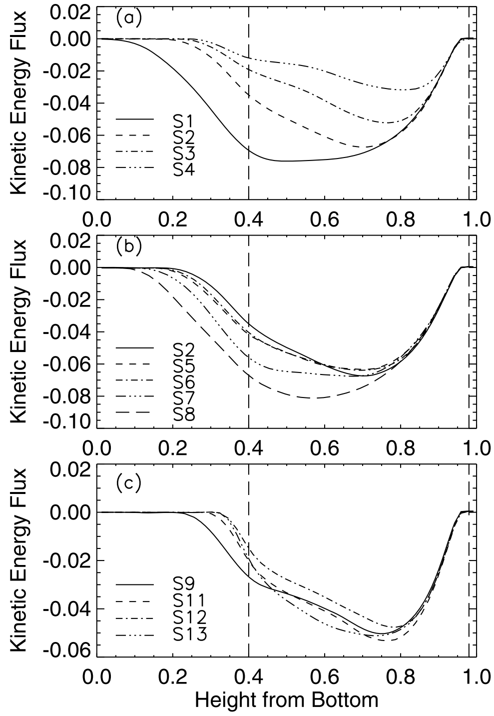

Fig. 3 Distribution of kinetic energy flux for models (**a**) *S1*, *S2*, *S3* and *S4*. The corresponding values of angular rotational velocity (**Ω**) are 0, 0.25, 0.50 and 1.0, respectively. For these *four cases* the angle (θ) between the rotation vector and the vertical axis is 0°, (**b**) *S2*, *S5*, *S6*, *S7* and *S8*. All these models have **Ω** fixed at 0.25 while θ changes from 0° to 90° in steps of 22.5°, (**c**) *S9*, *S11*, *S12* and *S13*. The polytropic indices in the lower stable layer for these four models are, respectively, 2, 3, 4 and 5. The corresponding relative stability parameters are 1, 3, 5 and 7, respectively. All the four models have $\mathbf{\Omega} = 0.5$ and $\theta = 45°$

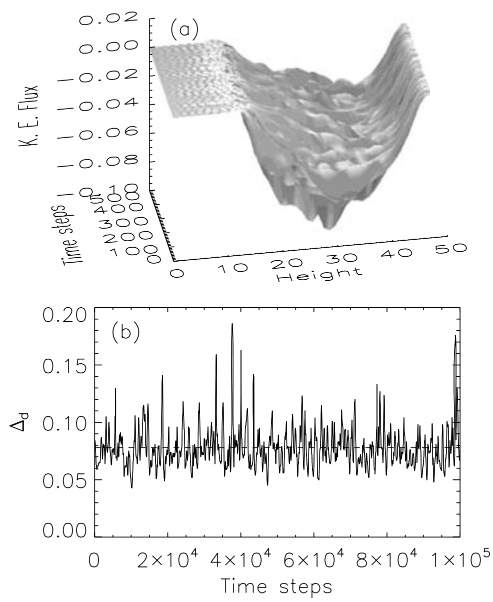

Fig. 4 (**a**) *Horizontally* averaged kinetic energy flux as a function of time. Total of 1,00,000 profiles were collected out of which 500 (every 200th) are plotted for case S13. The *height* is denoted in the grid points starting from one at the *bottom*. (**b**) Penetration depth (Δ_d) with time for model S13 for 1,00,000 time steps (computed at every 10th time step)

the penetration distance based on the corresponding averaged Kinetic energy flux. In Fig. 4a, we show the horizontally averaged kinetic energy flux as a function of depth and time for model S13. We have plotted 500 profiles of F_k out of these, corresponding to every 200th time step. In Fig. 4b, we show a time series of penetration distance Δ_d calculated by using the criterion outlined above. As can be seen, Δ_d is time dependent with a mean of 0.078 indicated by the horizontal dashed line. This agrees well with $\Delta_d = 0.077$ computed using a time- and horizontal-averaged kinetic energy flux for only 5000 time steps. Models S8 and S10 were also evolved for 1,00,000 time steps after thermal relaxation and the penetration depths are, respectively, 0.314 and 0.126 instead of 0.315 (S8) and 0.126 (S10) computed by averaging over 5000 time steps.

We now describe the effect of varying the three basic parameters **Ω**, θ, and S on the penetration depth.

3.1 Dependence of penetration depth on **Ω**

Two sets of models S1 to S4 and S6, S9 and S10 have been computed to examine the effect of rotation on the penetration distance. In models S1 to S4 the rotation rate (**Ω**) is systematically increased from 0.0 to 1.0 (Table 4). In these four models the rotation vector (θ) is 0°, implying that the rotation vector coincides with the Z-axis or the vertical direction. Figure 5a shows the dependence of penetration depth on **Ω**. In model S1, which is a non-rotating case ($\mathbf{\Omega} = 0$), the penetration distance $\Delta_d = 0.349$ or 1.08 PSH. As the rotation rate increases to 0.25 in model S2, Δ_d decreases to a distance of 0.214 which corresponds to 0.71 PSH. For models S3 and S4 having $\mathbf{\Omega} = 0.5$ and 1.0 respectively, the penetration depth decreases further to 0.61 PSH and 0.52 PSH respectively.

In the other set of models S6, S9 and S10, the rotation vector makes an angle of 45° with vertical direction and **Ω** is made to increase from 0.25 in model S6 to 0.5 in model S9. As can been seen from Table 4, the penetration depth (Δ_p) decreases from 0.77 PSH in model S6 to 0.61 PSH in model S9. For model S10, having the largest **Ω** at 1.0, the penetration distance is only 0.44 PSH.

In Figs. 6 and 7, we plot the pseudo-streamlines of the flow for the non-rotating case (S1) and for a rotating case (S10), respectively. Around 900 points are thrown into the fluid and the projections of the 3D flow are drawn on the XZ plane located at $Y = 0.6$. The presence of rotation-induced rolls is evident in the rotating case (Fig. 7). This results in the motions from the unstable layer penetrating the lower stable layer at an angle, resulting in a lower penetration in the rotating case. This effect is also clearly seen in Fig. 8

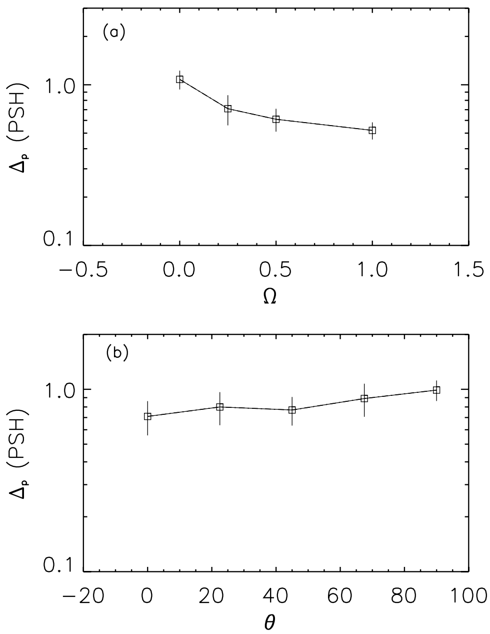

Fig. 5 Dependence of penetration depth Δ_p on (**a**) $\mathbf{\Omega}$ varying from 0, 0.25, 0.50 and 0.1 for the models S1, S2, S3 and S4 (**b**) colatitude (θ) varying from 0° to 90° in steps of 22.5° for models S2, S5, S6, S7 and S8 having $\mathbf{\Omega} = 0.25$. In this as well as in all the subsequent figures, error bars denote the standard deviation in Δ_p computed for 5000 time steps after the fluid has thermally relaxed

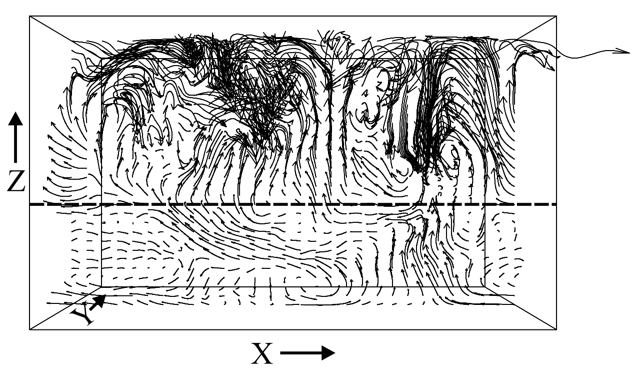

Fig. 6 Pseudo streamlines for an instantaneous velocity field of case S1 ($\mathbf{\Omega} = 0$) after the fluid is thermally relaxed. A total of 900 points are released from the XZ plane into the convecting fluid located at $Y = 0.6$. The dashed line shows the boundary located at $Z = 0.4$ between the middle unstable layer and the lower stable layer

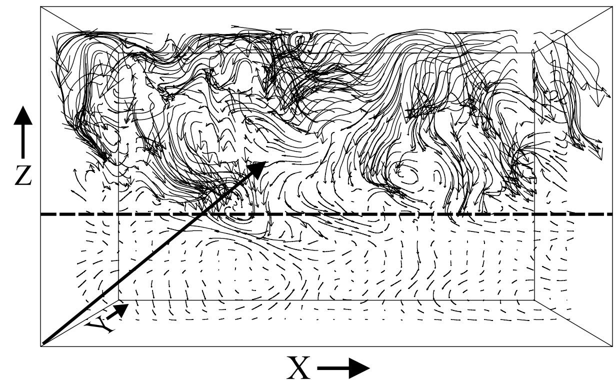

Fig. 7 Pseudo streamlines for an instantaneous velocity field of case S10 ($\mathbf{\Omega} = 1.0$, $\theta = 45°$) after the fluid is thermally relaxed. Projection is shown on the XZ plane located at $Y = 0.6$. The dashed line shows the boundary located at $Z = 0.4$ between the middle unstable layer and the lower stable layer. The long solid arrow shows the angular velocity vector. Alignment of the flow around the rotation vector is clearly visible

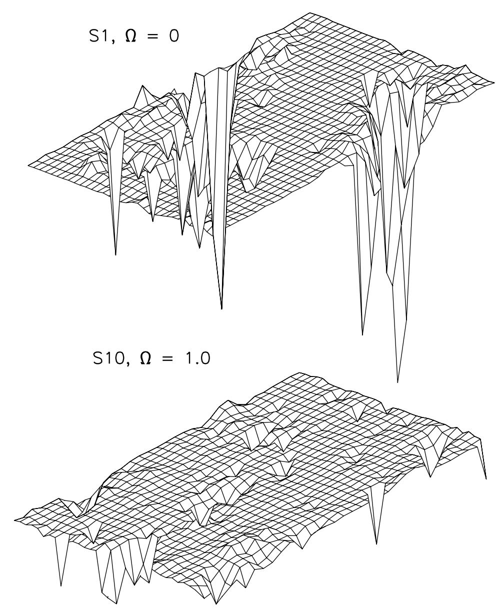

Fig. 8 Instantaneous flux of kinetic energy at a horizontal surface at unstable-lower stable layer boundary located at a height of 0.4 from the bottom for two cases *S1* ($\mathbf{\Omega} = 0$) and *S10* ($\mathbf{\Omega} = 1.0$, $\theta = 45°$)

in which we have plotted instantaneous kinetic energy flux for the same two models. The lower frame in Fig. 8 for the rotating model S10 clearly shows the absence of downward directed vertical plumes at the unstable layer-lower stable layer boundary.

3.2 Dependence of penetration depth on colatitude θ

A set of five models S2, S5, S6, S7 and S8 has been examined to study the effect of co-latitude (θ) on the penetration depth. All the models have $\mathbf{\Omega} = 0.25$ while θ is changed from 0° (Model S2) to 90° (Model S8) in steps of 22.5°. Figure 5b shows the plot of Δ_p against θ for the five models. At $\theta = 0°$, the penetration distance is 0.71 PSH. It increases for successive values of θ, except for $\theta = 45°$ where it dips slightly. A similar behaviour was observed by Brummell et al. (2002) except that they had dependence of penetration depth on latitude ϕ, which corresponds to our $(90° - \theta)$.

Figure 9a shows the variation of penetration depth Δ_p with Rossby number Ro for three cases S2, S3 and S4 having $\theta = 0°$ and $\Omega = 0.25$, 0.50 and 1.0, respectively.

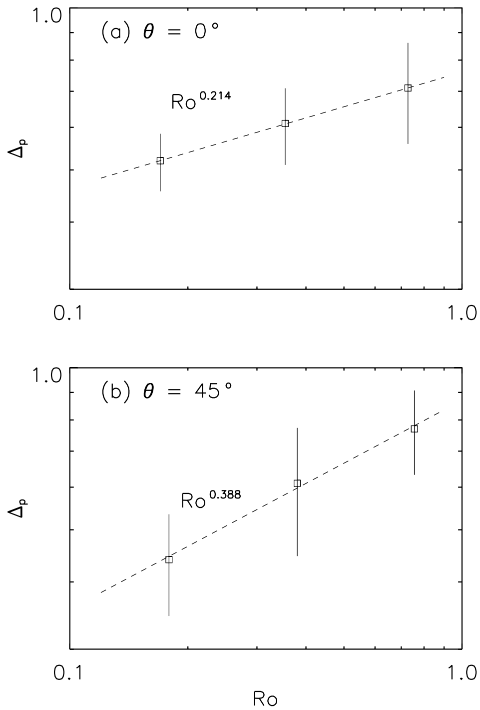

Fig. 9 Variation of penetration depth with Rossby number for (**a**) three models S2, S3 and S4 having $\mathbf{\Omega} = 0.25$, 0.50 and 1.0 respectively and $\theta = 0°$ and (**b**) three models S6, S9 and S10 having $\mathbf{\Omega} = 0.25$, 0.50 and 1.0 respectively and $\theta = 45°$. The *dashed lines* represent two scaling laws, $Ro^{0.214}$ and $Ro^{0.388}$

Since a smaller Rossby number implies a greater influence of rotation, the penetration depth decreases with decrease in the Rossby number of 0.728 for model S2 to 0.170 for model S4. For this set of models with $\theta = 0°$, we see a relationship $\Delta_p \sim 0.76Ro^{0.214}$. BCT02 have observed a relationship $\Delta_p \sim 0.26Ro^{0.15}$ for a set of three models with latitude $\phi = 90°$ which corresponds to our $\theta = 0°$ models.

Figure 9b shows the variation of Δ_p with Ro for another set of models S6, S9 and S10 with $\theta = 45°$ and $\Omega = 0.25$, 0.50 and 1.0, respectively. A similar behaviour is observed as Δ_p decreases with decrease in Ro of 0.756 for model S6 to 0.179 for model S9. A relationship $\Delta_p \sim 0.87Ro^{0.388}$ is observed for these set of models with $\theta = 45°$.

3.3 Dependence of penetration depth on relative stability parameter S

To examine the dependence of the penetration depth on the relative stability of the lower stable layer S as defined by (16), we have constructed four models with stability ratios $S = 1$, 3, 5 and 7 (cases S9, S11, S12 and S13). In Fig. 3c, we have plotted the distribution of the kinetic energy flux with depth for these four models. The values of the angular velocity ($\mathbf{\Omega}$) and angle (θ) between the rotation vector and vertical axis are fixed at 0.5 and 45°, respectively, for these four models. The corresponding penetration depths Δ_d and

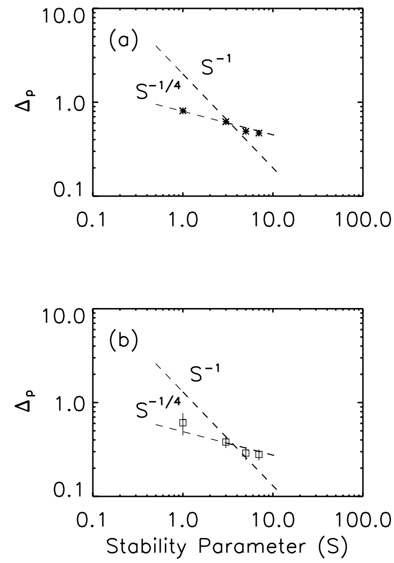

Fig. 10 Variation of penetration depth Δ_p with stability parameter S for (**a**) four non-rotating models of Singh et al. (1995) and (**b**) four rotating models S9, S11, S12 and S13. Here, $\mathbf{\Omega} = 0.5$ and $\theta = 45°$. The *dashed lines* represent two scaling laws, $S^{-1/4}$ and S^{-1}

Δ_p are given in Table 4. Figure 3c clearly shows the differences in the kinetic flux profile with S especially between the depth of 0.2 to a depth of 0.7 from the top. We, therefore, find a decrease in penetration depth from 0.61 PSH in model S9 ($S = 1$) to 0.28 PSH in model S13 ($S = 7$).

The 2D numerical simulations and related analytical calculations of Hurlburt et al. (1994) show that for smaller S the penetration depth (Δ_p) shows scaling S^{-1} associated with the presence of a nearly adiabatic overshoot region. For higher S they suggested a scaling of $S^{-1/4}$ associated with a thermal adjustment layer in the overshoot region. However, the high resolution 3D calculations of Brummell et al. (2002) find only a $S^{-1/4}$ dependence, even for higher values of S, suggesting the existence of a thermal adjustment region rather than a nearly adiabatic penetration zone.

Figure 10a shows the plots of penetration depth Δ_p with S for four non-rotating models of Singh et al. (1995) with $S = 1$, 3, 5 and 7. In Fig. 10b, we have shown the corresponding rotating models S9, S11, S12, and S13. We notice that Δ_p for the rotating cases are a bit lower than the values of Δ_p for the corresponding non-rotating cases. In both the figures, the penetration depth scales as $S^{-1/4}$. Although we do not achieve higher values of S, the behaviour is in agreement with Brummell et al. (2002).

4 Conclusions

We have presented the results of three-dimensional numerical simulations of turbulent compressible convection based on a series of 13 models. The models have been set up to examine the penetration of convective motions into the stable layer below under the influence of rotation. For the models under study, we find the penetration depth in the range $0.28\ \text{PSH} \leq \Delta_p \leq 1.08\ \text{PSH}$. We further find that the inclusion of rotation has the effect of reducing the penetration depth. In the non-rotating case, the downward plumes from the convection zone enter vertically into the lower stable layer. In the case of strong rotation, these downward directed plumes get aligned with the rotation vector and enter the lower stable layer at an angle, resulting in a lowering of the penetration depth.

We have also examined the effect of increasing the stability of the lower stable layer by increasing the relative stability parameter (S). We find that the penetration depth (Δ_p) scales as $S^{-1/4}$. This means that although the turbulent flows overshoot into the lower stable region for a considerable distance, they do not create a nearly adiabatic extension of the convection zone in the lower stable layer but rather give rise to a thermal adjustment region. We have been presently unable to perform more realistic simulations with parameter range close to the solar case due to the computational requirements of the problem, we have been able to get some insight into the dynamics of rotating convection at the interface of the convective-radiative interface at the bottom of a convective envelope.

Acknowledgements P.S.P. is grateful to University Grants Commission, India for a Junior fellowship. K.L.C. was partly supported by a grant from Hong Kong Research Grant Council. Authors acknowledge the use of High Performance Computing facilities at IUCAA, Pune, India.

References

Brummell, N.H., Hurlburt, N.E., Toomre, J.: Astrophys. J. **473**, 494 (1996)
Brummell, N.H., Clune, T.L., Toomre, J.: Astrophys. J. **493**, 955 (2002)
Chan, K.L.: Astrophys. J. **548**, 1102 (2001)
Chan, K.L.: In: Turcotte, S., Keller, S.C., Cavello, R.M. (eds.) Proc. Conf. on 3D Stellar Evolution, ASP Conf. Ser., vol. 293, p. 168. ASP, San Fransisco (2003)
Chan, K.L., Sofia, S.: Astrophys. J. **307**, 222 (1986)
Chan, K.L., Sofia, S.: Astrophys. J. **336**, 1022 (1989)
Chan, K.L., Sofia, S.: Astrophys. J. **466**, 372 (1996)
Chan, K.L., Wolff, C.L.: J. Comput. Phys. **47**, 109 (1982)
Deardorff, J.W.: J. Comput. Phys. **47**, 109 (1971)
Freytag, B., Ludwig, H.G., Steffen, M.: Astron. Astrophys. **313**, 497 (1996)
Hossain, M., Mullan, D.J.: Astrophys. J. **380**, 631 (1991)
Hossain, M., Mullan, D.J.: Astrophys. J. **416**, 733 (1993)
Hurlburt, N.E., Toomre, J.M., Massaguer, J.M.: Astrophys. J. **311**, 563 (1986)
Hurlburt, N.E., Toomre, J.M., Massaguer, J.M., Zahn, J.-P.: Astrophys. J. **421**, 245 (1994)
Käpylä, P.J., Korpi, M.J., Stix, M.J., Touminen, I.: Astron. Astrophys. **438**, 403 (2005)
Muthsam, H.J., Göb, W., Kupka, F., Leibich, W., Zöchling, J.: Astron. Astrophys. **293**, 127 (1995)
Rast, M.P., Nordlund, Å., Stein, R.F., Toomre, J.: Astrophys. J. **408**, L53 (1991)
Roxburgh, I.W., Simmons, R.: Astron. Astrophys. **347**, 734 (1993)
Saikia, E., Singh, H.P., Chan, K.L., Roxburgh, I.W., Srivastava, M.P.: Astrophys. J. **529**, 402 (2000)
Singh, H.P., Chan, K.L.: Astron. Astrophys. **279**, 107 (1993)
Singh, H.P., Roxburgh, I.W., Chan, K.L.: Astron. Astrophys. **281**, L73 (1994)
Singh, H.P., Roxburgh, I.W., Chan, K.L.: Astron. Astrophys. **295**, 703 (1995)
Singh, H.P., Roxburgh, I.W., Chan, K.L.: Bull. Astron. Soc. India **24**, 281 (1996)
Singh, H.P., Roxburgh, I.W., Chan, K.L.: In: Chan, K.L., Cheng, K.S., Singh, H.P. (eds.) Proc. 1997 Pacific Rim Conf. on Stellar Astrophysics, ASP Conf. Ser., vol. 138, p. 313. ASP, San Fransisco (1998a)
Singh, H.P., Roxburgh, I.W., Chan, K.L.: Astron. Astrophys. **340**, 178 (1998b)
Smagorinsky, J.S.: Mon. Weather Rev. **91**, 99 (1963)
Spiegel, E.A.: In: Rasool, S.I. (ed.) Physics of the Solar System, NASA, Washington (1972)
Spiegel, E.A., Zahn, J.-P.: Astron. Astrophys. **265**, 106 (1992)
Stein, R., Nordlund, Å.: In: Gough, D.O., Toomre, J. (eds.) Challenges to Theories of Moderate-Mass Stars, p. 195. Springer, Berlin (1991)
Thomson, M.J., The GONG Dynamics Inversion Team: Science **272**, 1300 (1996)